

Giant anomalous Hall effect in epitaxial $\text{Mn}_{3,2}\text{Ge}$ films with a cubic kagome structure

J. S. R. McCoombs¹, B. D. MacNeil¹, V. Askarpour¹, J. Myra¹, H. Herdin², M. Pula³, M. D. Robertson⁴, G. M. Luke³, K. L. Kavanagh², J. Maassen¹, and T. L. Monchesky^{1,*}

¹Department of Physics and Atmospheric Science, Dalhousie University, Halifax, Nova Scotia, Canada B3H 3J5

²Department of Physics, Simon Fraser University, Burnaby, British Columbia, Canada V5A 1S6

³Department of Physics and Astronomy, McMaster University, Hamilton, Ontario, Canada L8P 4N3

⁴Department of Physics, Acadia University, Wolfville, Nova Scotia, Canada B4P 2R6



(Received 1 November 2023; accepted 16 July 2024; published 1 August 2024)

We report on the first example of epitaxial $\text{Mn}_{3+\delta}\text{Ge}$ thin films with a cubic $L1_2$ structure. The films are found to exhibit frustrated ferromagnetism with an average magnetization corresponding to $0.98 \pm 0.06 \mu_B/\text{Mn}$, far larger than the parasitic ferromagnetism in hexagonal Mn_3Ge and the partially compensated ferrimagnetism in tetragonal Mn_3Ge . The Hall conductivity is the largest reported for the kagome magnets with a low-temperature value of $\sigma_{xy} = 1587 \text{ S/cm}$. Density functional calculations predict that a chiral antiferromagnetic structure is lower in energy than a ferromagnetic configuration in an ordered stoichiometric crystal. However, chemical disorder driven by the excess Mn in our films explains why a frustrated 120° spin structure is not observed. Comparisons between the magnetization and the Hall resistivity indicate that a noncoplanar spin structure contributes the Hall signal. Anisotropic magnetoresistance and planar Hall effect with hysteresis up to 14 T provides further insights into this material.

DOI: [10.1103/PhysRevB.110.064401](https://doi.org/10.1103/PhysRevB.110.064401)

I. INTRODUCTION

Magnetic topological metals offer opportunities to explore the entanglement of real-space and momentum space spin-structures. In Weyl semimetals formed by broken time-reversal symmetry, the real-space spin texture provides a way of manipulating the topological electronic states. In the case of the hexagonal Mn_3Sn and Mn_3Ge kagome materials, a rotation of the chiral antiferromagnetic spin configuration [shown in Fig. 1(b)] with an external magnetic field causes a rotation of the Weyl nodes [1]. The momentum-space Berry curvature in these structures leads to a large anomalous Hall effect (AHE) [2,3] and anomalous Nernst effect (ANE) [4,5] that have created opportunities for developing devices. The antiferromagnetic chiral structure of Mn_3Ge has also been used to manipulate spin-triplet Cooper pairs in a Josephson junction, with potential applications in superconductor logic circuits [6].

The closely related set of cubic kagome antiferromagnets Mn_3X , $X = \{\text{Ir}, \text{Pt}, \text{Rh}\}$ have a positive vector chirality [7–9] [see Fig. 1(e)], opposite to that of Mn_3Sn [10] and Mn_3Ge [11]. Their topological band structures give rise to large anomalous Hall [12,13] and spinHall effects [14]. The large uniaxial anisotropy in the case of Mn_3Ir leads to a canting of the spins out of the kagome planes and to a scalar spin chirality $\mathbf{S}_i \cdot (\mathbf{S}_j \times \mathbf{S}_k)$. However, it is spin-orbit coupling and broken mirror symmetry of the spin structure that gives rise to large momentum-space Berry curvature in this material [15].

In this paper we explore the properties of $\text{Mn}_{3,2}\text{Ge}$ films, which, in fact, has very similar hexagonal, cubic, and tetragonal polytypes with dramatically different magnetic properties. The phase that is obtained depends sensitively on the substrate and growth conditions. In bulk crystals, the hexagonal $\epsilon - \text{Mn}_3\text{Ge}$ phase ($D0_{19}$ crystal structure with space group #194, $P6_3/mmc$), is obtained by annealing at temperatures above 500°C [17,18]. The lattice parameters are $a_h = 0.534 \text{ nm}$ and $c_h = 0.431 \text{ nm}$ [17]. The Mn atoms occupy the $6h$ Wyckoff sites and form an AB-stacking of kagome layers with their spins pointing in the plane at an angle of 120° to their neighbors [19]. This order exists below a Curie temperature of 365 K [18]. The in-plane easy axis magnetocrystalline anisotropy induces a weak moment of $0.007 \mu_B \text{ Mn}^{-1}$ [18] in the kagome plane [11]. Epitaxial $\text{Mn}_{3,22}\text{Ge}(0001)$ films were achieved on sapphire (0001) substrates with a Ru buffer layer by co-sputtering Mn and Ge at a rate of 10 nm/min and subsequent annealing at 500°C [5], as well as by molecular-beam epitaxy on $\text{LaAlO}_3(111)$ at a temperature of 570°C [20].

Tetragonal $\epsilon_1 - \text{Mn}_3\text{Ge}$ [$D0_{22}$ crystal structure with space group #139, $I4/mmm$ shown in Fig. 1(d)] is the thermodynamically stable phase below 500°C , which possesses ferrimagnetic order with spins parallel to the c axis [17] and an estimated Curie temperature of 650°C [19]. This phase, with lattice parameters $a_t = 0.3816 \text{ nm}$ and $c_t = 0.7216 \text{ nm}$ [19], grows epitaxially on $\text{SrTiO}_3(001)$, which has a lattice parameter 2.3% larger than the a parameter [21]. Epitaxial films have also been grown on $\text{MgO}(001)$ with a Cr buffer layer [22]. The films have strongly compensated moments with a net magnetization $M_s = 73 \text{ kA/m}$, and a very high uniaxial anisotropy $K_u = 0.91 \text{ MJ/m}^3$ despite the absence of heavy elements. The tetragonal phase can be transformed into

*Contact author: tmonches@dal.ca

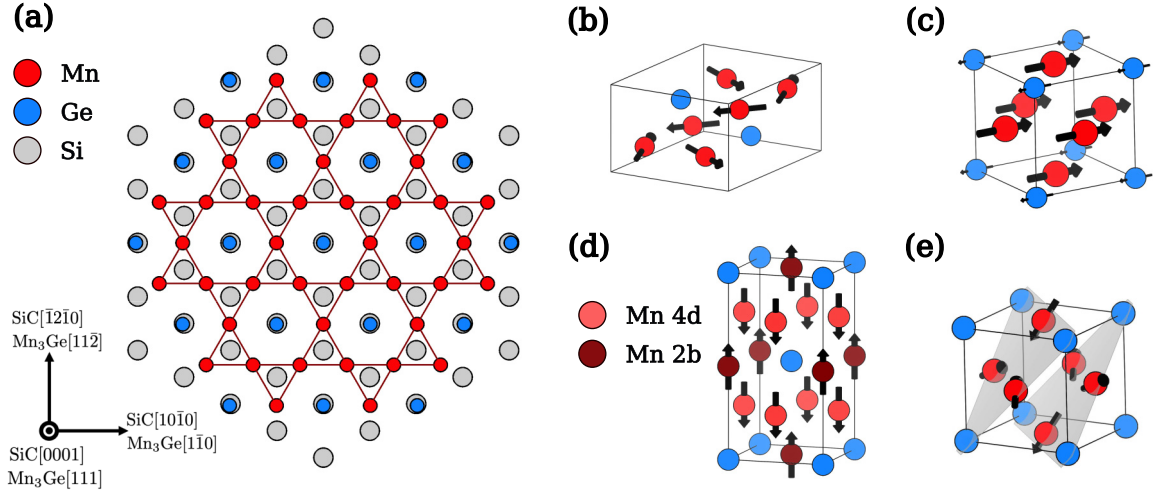


FIG. 1. (a) The expected epitaxial relationship of L_{12} Mn₃Ge atop SiC. (b) The crystal structure and inverse-triangular, AFM spin-configuration of hexagonal D_{019} Mn₃Ge. (c) The crystal structure and DFT calculated ferromagnetic spin-configuration of cubic L_{12} Mn₃Ge. (d) The crystal structure and ferrimagnetic spin-configuration of D_{022} Mn₃Ge. (e) The cubic L_{12} structure with DFT calculated triangular, AFM spin-configuration. Images generated with VESTA [16].

the cubic variant by stretching the unit cell by 5% along the c axis and interchanging one of the Ge atoms on the $2a$ sites with one of the Mn atoms on the $2b$ sites. In this way, the tetragonal phase can be viewed as a distorted ABC-stacked kagome structure.

Cubic Mn₃Ge (L_{12} structure with space group #221, $Pm\bar{3}m$) differs from the hexagonal phase only in its ABC-stacking of the kagome layers. The Mn atoms sit on the $3c$ Wyckoff sites, corresponding to the cubic unit cell faces. There is only one report to date on the synthesis of this material, which was achieved by reacting Mn and Ge at high temperatures and pressures [23]. The cubic lattice parameter $a = 0.3802(1)$ nm is close to both the a_t and $a_h/\sqrt{2}$ parameters. However, the magnetic properties are quite different: magnetometry measurements revealed ferromagnetic behavior, with a saturation magnetization that corresponds to $0.87 \mu_B \text{ Mn}^{-1}$ and a Curie temperature, T_C , of approximately 400 K. Here, we report the first demonstration of the growth of cubic Mn_{3+ δ} Ge films. We used 4H-SiC(0001) substrates, which have a -0.75% lattice mismatch.

The rest of this paper is structured as follows: We first describe the growth procedure and outline the structural experiments we conducted which lead us to the conclusion that we have an epitaxial, cubic kagome system. We probe the spin-configuration in this system with complementary in-plane and out-of-plane magnetometry and DC transport measurements. Finally, we present a density functional theory (DFT) investigation of the ground-state spin structure of stoichiometric Mn₃Ge and the resulting Berry curvature.

II. GROWTH

We used 4H-SiC(0001) $\pm 0.5^\circ$ Si-terminated wafers with a resistivity of $\approx 1 \times 10^5 \Omega \text{ cm}$ as substrates. Prior to growth, these substrates were degassed in acetone and methanol, rinsed in deionized water, dried with nitrogen, then immediately loaded into a VG-V80 SiGe molecular-beam epitaxy

(MBE) chamber with a base pressure of less than 4×10^{-11} Torr. The substrates were then degassed at 600°C for 12 hr, followed by flashing to 1100°C for 1 hr to remove the SiO₂ layer. This process results in a $(\sqrt{3} \times \sqrt{3})R30^\circ$ surface reconstruction free of any oxygen, as evinced by *in situ* reflection high-energy electron diffraction (RHEED) and Auger-electron spectroscopy (AES). The substrate is then cooled at a rate of approximately $20^\circ \text{C}/\text{min}$ to room temperature, T_R , for co-deposition of Mn via effusion cell and Ge via electron-beam evaporation. Upon reaching T_R , Mn and Ge are deposited at an atomic ratio of 5 : 1. The Mn rate is monitored with a calibrated ion gauge, while the Ge rate is monitored with a quartz oscillator. Upon completion of co-deposition, the sample is heated to 600°C for 1 hr while monitored with RHEED until diffraction spots are recovered. The temperature of 600°C was chosen since it was found that lower temperatures led to smoother films. However, temperatures up to $\approx 550^\circ \text{C}$ did not crystallize. Thus, 600°C seems to be near the lowest temperature which results in a crystallized film.

Due to Mn evaporation from the film at elevated substrate temperatures, a ratio Mn : Ge = 5 : 1 was required to achieve the desired stoichiometry, as evinced by energy dispersive x-ray spectroscopy (EDS). For this reason, we use the total deposited thickness of Ge as a calibration of the expected thickness of our Mn₃Ge films. The number density of elemental Ge is $n_{\text{Ge}}^{\text{Ge}} = 0.04412 \text{ \AA}^{-3}$, while the number density of Ge in Mn₃Ge is $n_{\text{Mn}_3\text{Ge}}^{\text{Ge}} = 0.0182 \text{ \AA}^{-3}$. Hence, for a thickness of t_{Ge} deposited we expect a thickness of

$$t_{\text{Mn}_3\text{Ge}} = \frac{n_{\text{Ge}}^{\text{Ge}}}{n_{\text{Mn}_3\text{Ge}}^{\text{Ge}}} \frac{t_{\text{Ge}}}{\alpha} \quad (1)$$

for our film, where $\alpha = 0.8$ accounts for the remaining excess Mn occupying Ge sites. Lastly, before removing the sample from the MBE, it is again cooled to T_R for the deposition of a 10 nm protective, amorphous layer of Si.

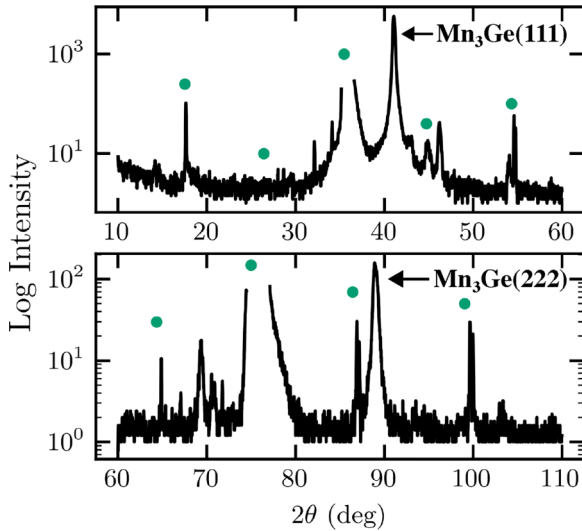


FIG. 2. Log-scale plot of traditional $\theta - 2\theta$ diffraction pattern using Cu-K α x-rays. The SiC(0004) and SiC(0008) reflections are omitted. Green circles indicate positions of allowed and forbidden SiC(000 l) reflections.

III. STRUCTURAL AND CHEMICAL CHARACTERIZATION

A. Diffraction

After aligning the SiC(0004) reflection along the q_z axis of the Siemens D500 x-ray diffractometer, traditional $\theta - 2\theta$ measurements are performed using a Cu source and monochromator which allows only Cu K- α wavelengths. Figure 2 shows the diffraction pattern obtained exhibiting only two film peaks with appreciable intensity and indicating a plane spacing of 2.196 Å for planes parallel with the surface of the film. Aside from the clear Mn₃Ge(111) and (222) peaks, there are some small [$<1\%$ of the Mn₃Ge(111) intensity] peaks present which are made visible by the log scale of Fig. 2. These peaks could be due to the presence of either small amounts of other Mn₃Ge orientations or small amounts of other Mn-Ge phases. The predominant alignment of the film is consistent with the expected epitaxial relationship of Mn₃Ge atop SiC. A cubic system with lattice parameter 0.3803 nm [as obtained by the (111) plane spacing] should have an in-plane, pseudohexagonal lattice parameter of $a_h = \sqrt{2}a = 0.5336$ nm [24]. This unit-cell dimension is accommodated on the SiC(0001) surface by considering a $(\sqrt{3} \times \sqrt{3})R30^\circ$ -type epitaxy which leads to the expected relationship

$$[1\bar{1}0]\text{Mn}_3\text{Ge}(111) \parallel [10\bar{1}0]\text{SiC}(0001). \quad (2)$$

This expected alignment is shown in Fig. 1, which also highlights that there should be a compressive strain on the film since its in-plane lattice parameter is 0.80% larger than that of the SiC $R30^\circ$ cell.

It is important to note that the plane-spacing of the cubic Mn₃Ge(111), hexagonal Mn₃Ge(0001), and tetragonal Mn₃Ge(112) families of planes are all very similar and would therefore have very similar diffraction patterns when scanning along the q_z direction. To rule out these other polytypes we

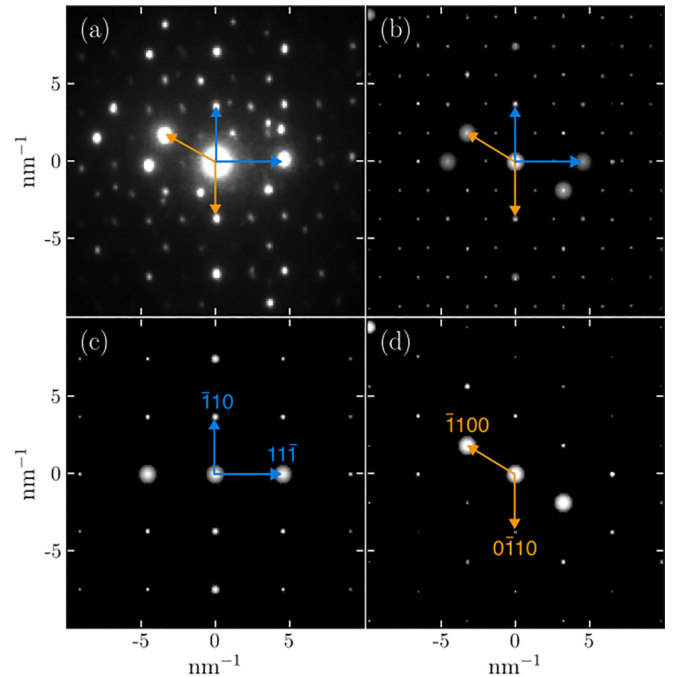


FIG. 3. (a) Experimental TEM selected area diffraction pattern and (b) simulated pattern for a 44 nm Mn₃Ge layer atop a 44 nm SiC layer with double diffraction spots included, obtained from a sample tilted by 19.5 degrees about the Mn₃Ge [110] in-plane direction to align with the Mn₃Ge [112] zone axis. Panels (c) and (d) show simulated patterns from the Mn₃Ge and SiC layers, respectively.

conducted further diffraction experiments to gain in-plane information about the film.

Transmission electron microscopy (TEM) plan-view samples were prepared by low-angle mechanical polishing and attached to TEM grids with silver epoxy [25]. A selected area diffraction pattern (SADP) was obtained using a 200 kV field-emission microscope after the sample was rotated 19.5° about the Mn₃Ge[$1\bar{1}0$] so as to be aligned with the Mn₃Ge(112) zone axis. Along this zone axis, clear distinction between diffraction patterns owing to the film and to the SiC substrate can be made which support the epitaxial relationship described in Eq. (2). Figure 3 shows the experimental SADP along with a simulated pattern which was obtained using the Bloch-wave method [26]. Good agreement is observed and peaks can be identified by the individual simulated patterns of Mn₃Ge and SiC. Additional peaks that do not appear in the individual Mn₃Ge or SiC simulations but do appear in the stacked simulation are due to electrons that have diffracted in both the film and substrate. These double diffraction spots also match well with the experiment.

As further evidence of the cubic structure of our film and the epitaxial relationship given in Eq. (2), we explore the reciprocal space map (RSM) of our films again using Cu K- α x rays. To distinguish between the two primary, perpendicular, in-plane directions we denote the direction along SiC[$\bar{1}2\bar{1}0$] \hat{x} and the direction along SiC[$\bar{1}010$] \hat{y} , with the direction along SiC[0001] reserved for \hat{z} . Figure 4 shows a portion of the (q_x, q_z) reciprocal space highlighting the (311) and (211) cubic peaks, which correspond to

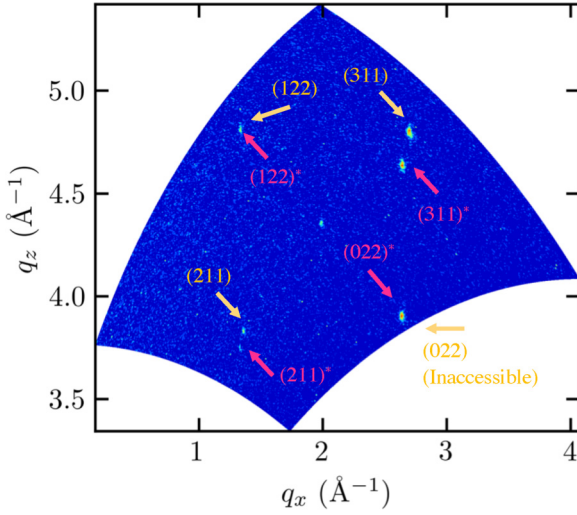


FIG. 4. Reciprocal space map of the (q_x, q_z) plane. Gold, unstarred labels represent diffraction spots from the perfectly cubic system with lattice parameter 0.3803 nm. Magenta, starred labels represent diffraction spots from a cubic system stretched along the $[100]$ direction by 3%.

$[2\bar{1}\bar{1}]Mn_3Ge(111)||[\bar{1}\bar{2}\bar{1}0]SiC(0001)$ regions of the film, as well as the (022) and (122) peaks, which correspond to $[2\bar{1}\bar{1}]Mn_3Ge(111)||[\bar{1}\bar{2}\bar{1}0]SiC(0001)$ regions of the film. The remaining peaks are surmised to be due to a distortion of the perfect cubic structure along the $[100]$ direction. The direction of the distortion is consistent with the $[001]$ direction of a (112)-oriented $D0_{22}$ film atop SiC. However, the RSM can only be explained by a *stretching* of the cubic cell along $[100]$, with a resulting c/a ratio of 2.07, which is opposite to the distortion of $D0_{22}$ Mn_3Ge with $c/a = 1.90$. Simulated RSM patterns were prepared with the aid of the open-source software XRAYUTILITIES [27] and are shown in Fig. 5. These simulations motivate the portion of reciprocal space probed. In particular, the pattern with $q_x || [2\bar{1}\bar{1}]Mn_3Ge(111)||[\bar{1}\bar{2}\bar{1}0]SiC(0001)$ can be used to verify the epitaxial relationship since the film peaks are well separated from the substrate peaks. Conversely, with $q_y || [1\bar{1}0]Mn_3Ge(111)||[1\bar{1}00]SiC(0001)$, the film peaks are closely aligned with the far higher intensity substrate peaks making this orientation far less useful.

B. Microscopy

Scanning transmission electron microscopy (STEM) images were collected with a 200 kV field-emission microscope using the same sample as mentioned previously. Figure 6(a) shows the presence of holes in the film: EDS showed no Mn or Ge in these regions. In the other regions of the sample, EDS found that the film has an excess of Mn with a ratio of Mn : Ge = 3.2(0.2) : 1.

Surface morphology was investigated with atomic-force microscopy (AFM). The surface is revealed to be largely continuous with some holes that extend to the substrate [Fig. 6(b)], as seen in the STEM results. It should be noted that the roughness of these films is very large compared with examples of the hexagonal polytype atop $LaAlO_3$ [5] and

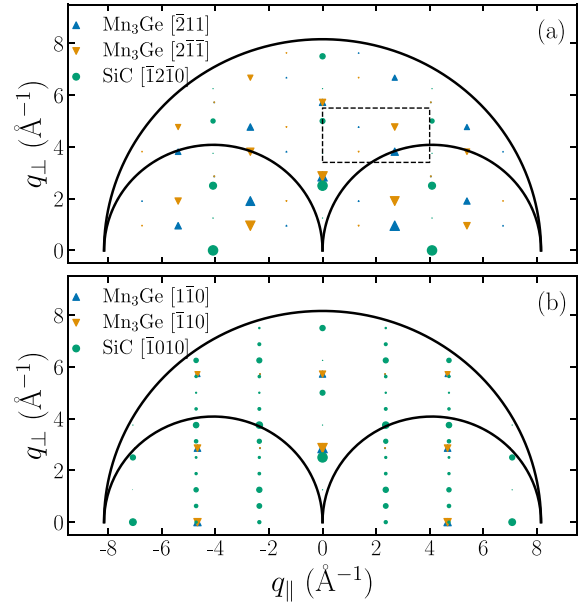


FIG. 5. Simulated RSM's with (a) $q_{||} = q_x || [2\bar{1}\bar{1}]Mn_3Ge(111) || [\bar{1}\bar{2}\bar{1}0]SiC(0001)$ and (b) $q_{||} = q_y || [1\bar{1}0]Mn_3Ge(111)||[1\bar{1}00]SiC(0001)$. The curved, solid, black lines indicate the area of reciprocal space accessible by a standard diffractometer while the solid black box indicates the region of reciprocal space shown in Fig. 4.

Al_2O_3/Ru [20]. We attribute this roughness to the choice of SiC substrate. Even though the lattice mismatch is extremely small, we expect large differences in surface energies have hindered wetting of the film in a similar manner as was observed in growth of the helimagnet MnSi on SiC [28]. The AFM topographical map gives root-mean-squared roughness of 31.9 nm and a corresponding nominal thickness of 43.9 nm. This thickness is consistent with the peak widths of the (111) and (222) reflections measured in the $\theta - 2\theta$ x-ray diffraction scan. It is also consistent with the nominal amount of Ge deposited as described by Eq. (1) if $\alpha = 0.8$, which matches the EDS measurement.

IV. MAGNETOMETRY AND TRANSPORT

The following magnetometry measurements reveal that the magnetic structure of the cubic films is distinctly different

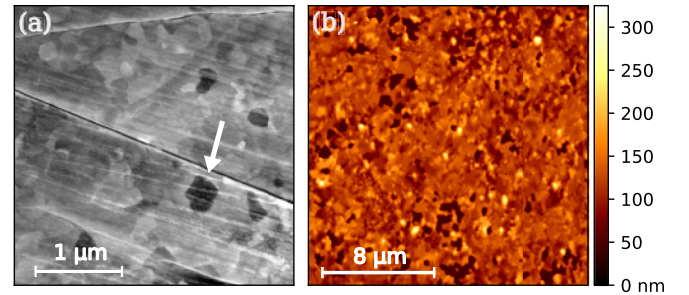


FIG. 6. (a) HAADF-STEM image revealing the film island morphology from the white and gray contrast. The arrow points to one of the darker regions where the SiC was exposed. A crack running through the tip of the arrow resulted from the mechanical polishing. (b) AFM of the film surface showing the distribution of holes.

from the other two polytypes. The out-of-plane (OOP) magnetization uncovers a compensation point in the remanent magnetization, indicative of a ferrimagnetic behavior. The corresponding Hall-effect measurements provide further insights into the spin structure. We also present in-plane (IP) magnetotransport measurements that show a large anisotropy that derives from the cubic lattice.

Out-of-plane magnetization measurements were performed with a Quantum Design MPMS SQUID magnetometer in the traditional RSO mode with a maximum applied field of 7 T. Transport measurements were performed on a Quantum Design Dynacool PPMS with a maximum applied field of 14 T. For transport measurements, samples were cleaved into $\approx(6 \times 1)$ mm rectangles with constant-current-supplying leads I^+ , I^- , transverse voltage leads V_{xy}^+ , V_{xy}^- , and longitudinal voltage leads V_{xx}^+ , V_{xx}^- wire-bonded to the surface using 20 μm aluminum wire. Five constant current leads are used such that the electric field is highly uniform in the region where the voltage leads are attached, as verified by the numerical solution of Poisson's equation for this geometry.

A. Out-of-plane field

Figure 7 shows $M - H$ and the antisymmetrized $\rho_{xy} - H$ hysteresis loops at various temperatures ranging from 400 K down to 10 K. The linear, diamagnetic susceptibility of the SiC substrates and the linear, conventional Hall effect have been subtracted away from the presented data. It should be noted that, although there appears to be saturation in $\rho_{xy}(H)$ for all temperatures considered, there is a small nonlinearity that persists up to 14 T which becomes less prevalent as temperature is reduced.

Figure 8 shows the difference between the field-decreasing branch of the hysteresis loops and the field-increasing branch. Clear deviation between the behavior of $\rho_{xy}(H)$ and $M(H)$ is observed. These differences are summarized in Fig. 9. While the coercive field H_C , saturation M_S , and remanent M_R of the magnetization are all monotonically increasing with decreasing temperature, the complementary values of ρ_{xy} show a more complex dependence. Notably, at ≈ 250 K, there is a sharp decrease in the remanent Hall resistivity, ρ_{xy}^R , and a change in character of $\Delta\rho_{xy}$. The significance of this temperature is highlighted in zero-field-warming (ZFW) measurements of the remanent OOP magnetization. Field cooling at 7 T (-7 T) followed by ZFW shows a ferromagnetic-type behavior up to $T_{C1} = 260$ K, followed by a magnetization reversal above T_{C1} (see Fig. 10). This is contrary to the strictly positive (negative) remanent moments derived from the isothermal hysteresis loops above. We attribute this reversal to an antiferromagnetic coupling between Mn moments on the 3c sites with Mn moments on the Ge 1a sites leading to a ferrimagnetic-like behavior. This thermally onset transition is also observed in field-cooled and field-warmed scans at various values of $\mu_0 H$, manifesting as a spike in dM/dT and moving to slightly higher temperatures as the external field increases. At low fields, there is substantial thermal hysteresis which recedes as the applied field increases in magnitude.

A more comprehensive investigation of the temperature dependence of ρ_{xy} was achieved by field cooling at 5 T and zero-field warming resulting in a temperature dependence

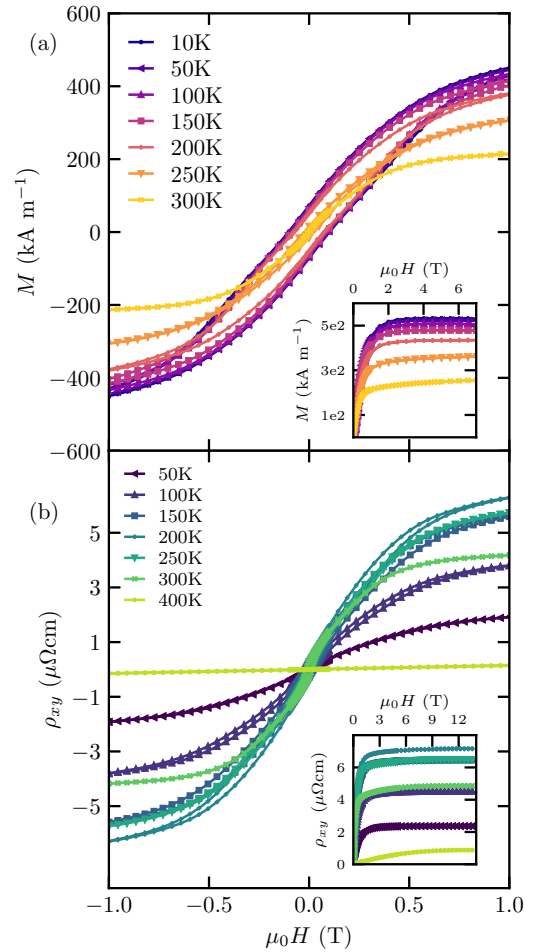


FIG. 7. (a) Magnetization hysteresis loops with external field parallel to SiC[0001]. The diamagnetic susceptibility of the SiC substrate has been subtracted. (b) Antisymmetrized transverse resistivity hysteresis loops with external field parallel to SiC[0001]. The conventional, linear Hall effect has been subtracted. Insets show the high-field behaviors of M and ρ_{xy} .

$\rho_{xy}^{0+}(T)$ followed by field cooling at -5 T and zero-field warming resulting in a temperature dependence $\rho_{xy}^{0-}(T)$. By examining $\rho_{xy}^R = [\rho_{xy}^{0+}(T) - \rho_{xy}^{0-}(T)]/2$, we obtain the remanent transverse resistivity as a function of T . This temperature dependence is shown in Fig. 11, along with the temperature dependence of ρ_{xx} at zero field. Possibly due to the higher maximum temperature of this measurement, the remanent $\rho_{xy}^R(T)$ on zero-field-warming exhibits no discernible feature at T_{C1} and is substantially higher than the remanent values obtained from the hysteresis loops in Fig. 7. Instead, after peaking at 200 K, it linearly decreases until it abruptly approaches zero at $T_{C2} = 377$ K, comparable to the $T = 400$ K reported in bulk cubic crystals [23]. The sharp peak in $d\rho_{xy}^R/dT$ at T_{C2} indicates the onset of a remanent magnetization and provides an estimate for the Curie temperature. This temperature could not be confirmed with the SQUID measurements because of the temperature limit of the sample holder for this instrument, but the presence of a remanent magnetization in SQUID at 300 K places a lower bound for the onset of magnetic order.

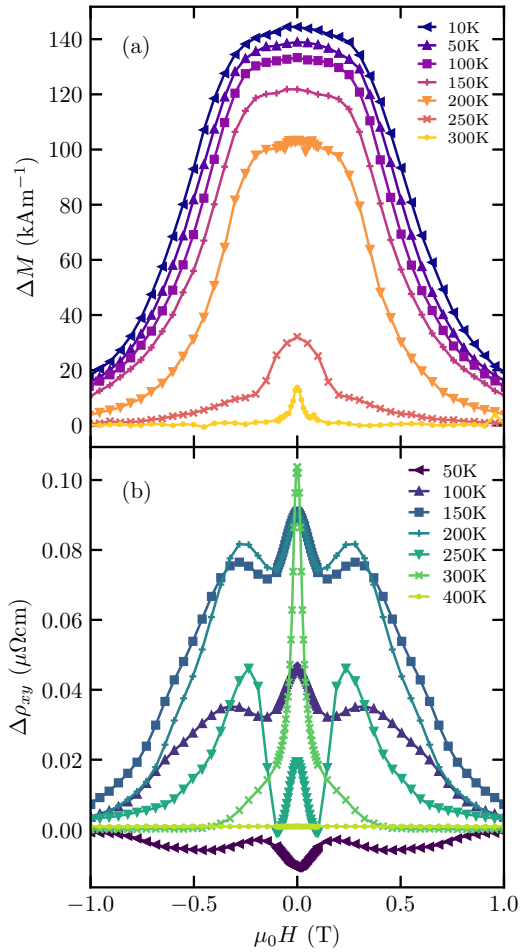


FIG. 8. Differences between the field-decreasing and field-increasing (a) magnetization and (b) transverse resistivity extracted from the isothermal hysteresis loops presented in Fig. 7.

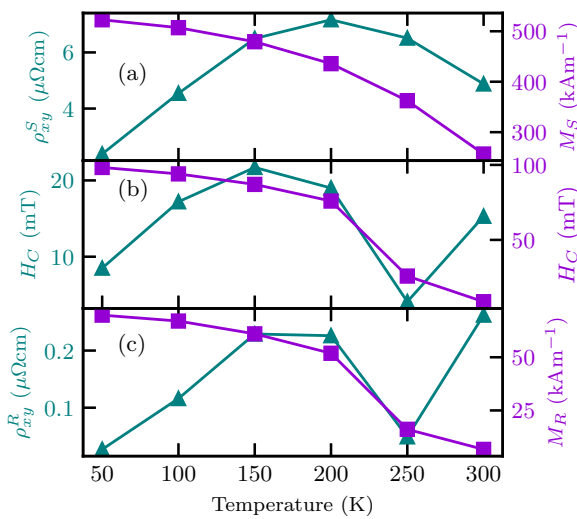


FIG. 9. Temperature dependence of (a) saturation magnetization (M_S) and saturation transverse resistivity ρ_{xy}^S , (b) coercive fields of M and ρ_{xy} , and (c) magnetization M_R and remanent transverse resistivity ρ_{xy}^R . All quantities were extracted from the series of isothermal hysteresis loops shown in Fig. 7.

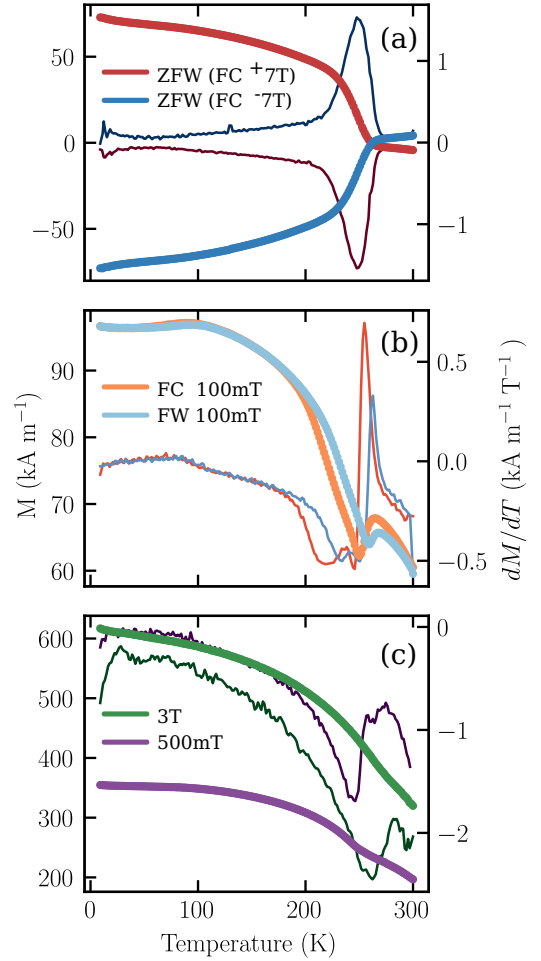


FIG. 10. (a) ZFW curves and their derivatives after field cooling in a 7 T and -7 T field. (b) 100 mT field-cooled (FC) and field-warmed (FW) curves and their derivatives showing clear thermal hysteresis. (c) 500 mT and 3 T FC curves and their derivatives. In all plots, the left axis corresponds to the thick $M(T)$ curves while the right axis corresponds to the thin $dM(T)/dT$ curves.

B. Field in plane

For in-plane measurements, the sample was mounted to a rotating stage in a manner outlined in the inset of Fig. 12(a). The angle the external field makes with the direction of the current density \mathbf{J} and hence the $\text{SiC}[2\bar{1}\bar{1}0]$ direction will be defined as ψ .

Isothermal longitudinal magnetoresistance (LMR) and planar Hall effect (PHE) hysteresis loops were conducted at various temperatures, as shown in Fig. 13. These measurements were performed with $\psi = 0^\circ$, such that the field was along the direction of the current density. Negative LMR is observed for all temperatures, with hysteresis beginning to show at 100 K and growing as the temperature is reduced to 5 K. There is a small, time-reversal-antisymmetric portion of the PHE with a coercive field of around 0.01 T at 300 K and growing to around 0.08 T at 50 K. This could be attributed to a small misalignment of the film, leading to a component of the OOP Hall effect imparting a contribution.

Anisotropic magnetoresistance (AMR) [$\rho_{xx}(\psi)$] and PHE [$\rho_{xy}(\psi)$] were explored by rotating the angle ψ through 380°

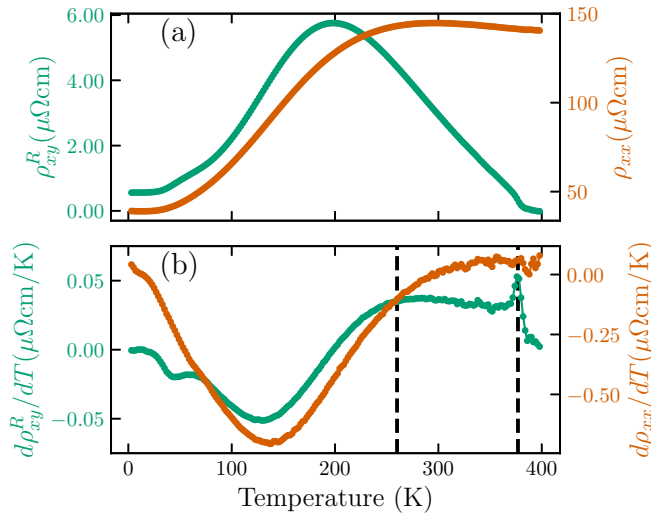


FIG. 11. Temperature dependence of (a) ρ_{xy}^R and ρ_{xx} upon warming after field-cooling at 5 T and (b) the derivatives of ρ_{xy}^R and ρ_{xx} . Vertical lines have been added at the temperatures $T_{C1} = 260$ K and $T_{C2} = 377$ K

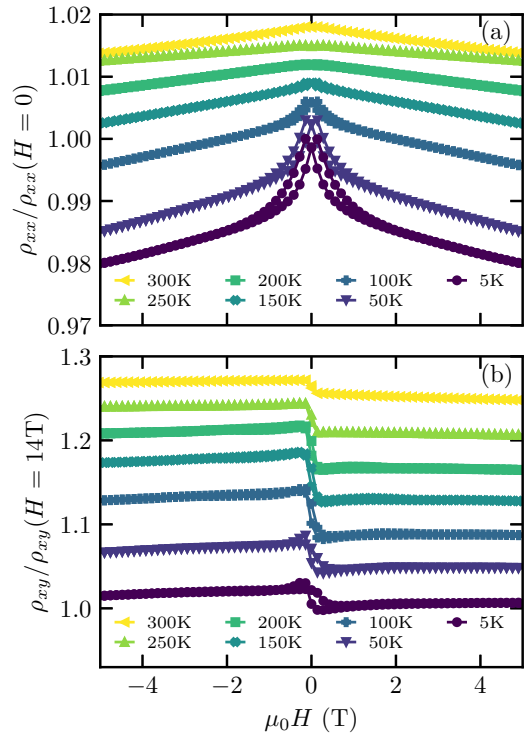


FIG. 13. Constant-temperature hysteresis loops of (a) LMR and (b) PHE. These measurements were performed with the applied field parallel to the current density, $\psi = 0^\circ$. The data have been offset vertically for clarity.

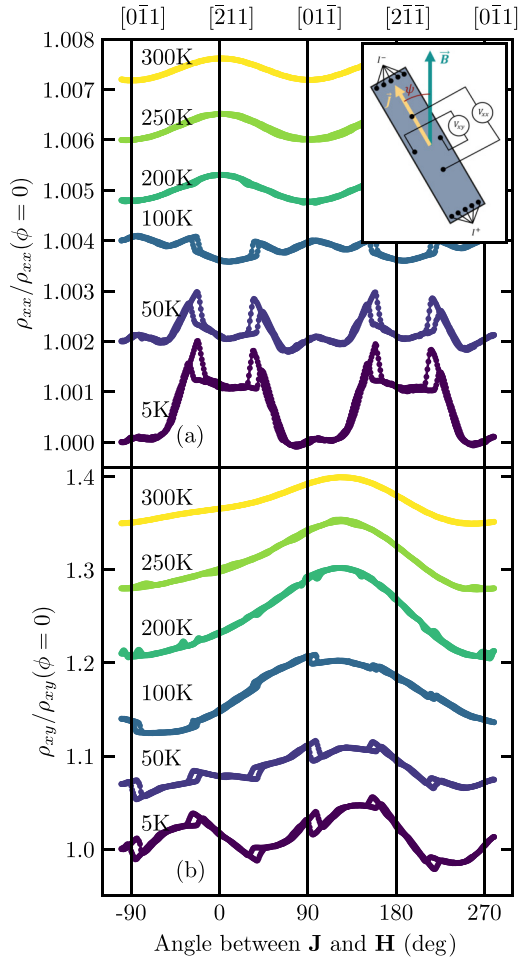


FIG. 12. Constant temperature scans of (a) AMR, $\rho_{xx}(\psi)/\rho_{xx}(\psi = 0)$ and (b) PHE, $\rho_{xy}(\psi)/\rho_{xy}(\psi = 0)$ at $\mu_0H = 3$ T. The inset of panel (a) shows the experimental geometry.

(from -100° to 280°) first at various temperatures with a constant applied field $\mu_0H = 3$ T as shown in Fig. 12. At 300 K, typical AMR behavior is observed with $\rho_{xx} \propto \cos^2(\psi)$ and $\rho_{xy} \propto \sin(2\psi)$. However, upon cooling, clear hysteresis arises, with discontinuous jumps occurring in both ρ_{xx} and ρ_{xy} at intervals of $\approx 60^\circ$. This change in behavior from high to low temperature is captured with Fourier analysis of the AMR or PHE, as shown in Fig. 14. At higher temperatures, the conventional, twofold rotational symmetry is dominant, but as temperature falls, other even Fourier components contribute,

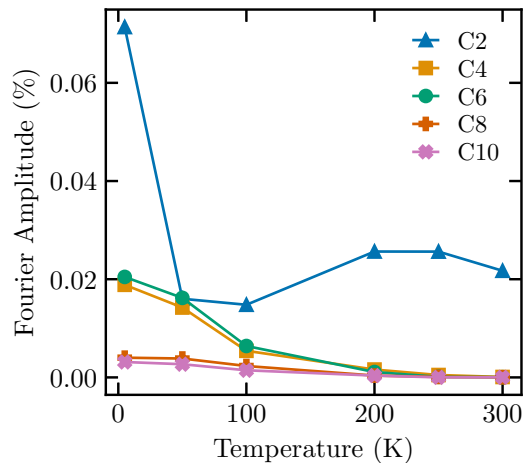


FIG. 14. Relative Fourier components of the average AMR for angle increasing and angle decreasing as a function of temperature at a constant field of $\mu_0H = 3$ T.

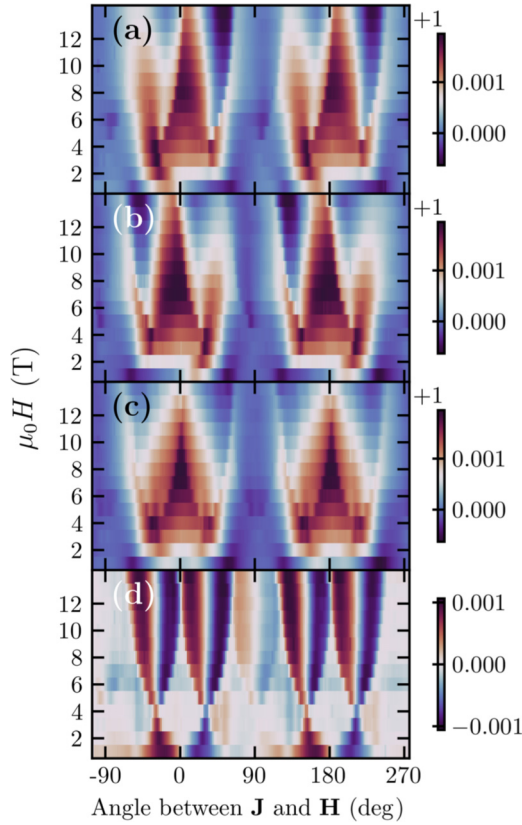


FIG. 15. AMR, $\rho_{xx}(\psi)/\rho_{xx}(\psi = 0)$ for (a) ψ increasing, (b) ψ decreasing, (c) the average of increasing and decreasing, and (d) the difference between increasing and decreasing.

with sixfold and fourfold components the primary among them.

To further examine the low-temperature, unconventional AMR or PHE, rotation measurements were performed with varying applied fields at a constant temperature of 5 K. These are shown in Figs. 15 and 16. Clear hysteresis is present for all fields considered, with the discontinuous jumps present at 60° intervals appearing to be amplified and smeared out into more continuous transitions as the field is increased. The difference between angle-increasing and angle-decreasing AMR and PHE shows a very clear sixfold rotational symmetry, as is captured by the Fourier analysis shown in Fig. 17.

V. DENSITY FUNCTIONAL THEORY CALCULATIONS

A. Computational details

The density functional theory (DFT) simulations were carried out with the Vienna *ab initio* Simulation Package (VASP) [29] within the generalized gradient approximation (GGA) [30] and the projector augmented wave (PAW) method [31]. The calculations included a noncollinear treatment of the magnetization, spin-orbit coupling, and the removal of symmetry recognition. The following simulation parameters were adopted: kinetic-energy cutoff of 700 eV, Monkhorst-Pack [32] Brillouin-zone \mathbf{k} sampling of $10 \times 10 \times 10$ for the cubic phase and $8 \times 8 \times 8$ for the hexagonal phase, Methfessel-Paxton smearing [33] of 0.15 eV, electronic energy convergence of 10^{-8} eV, and relaxation energy con-

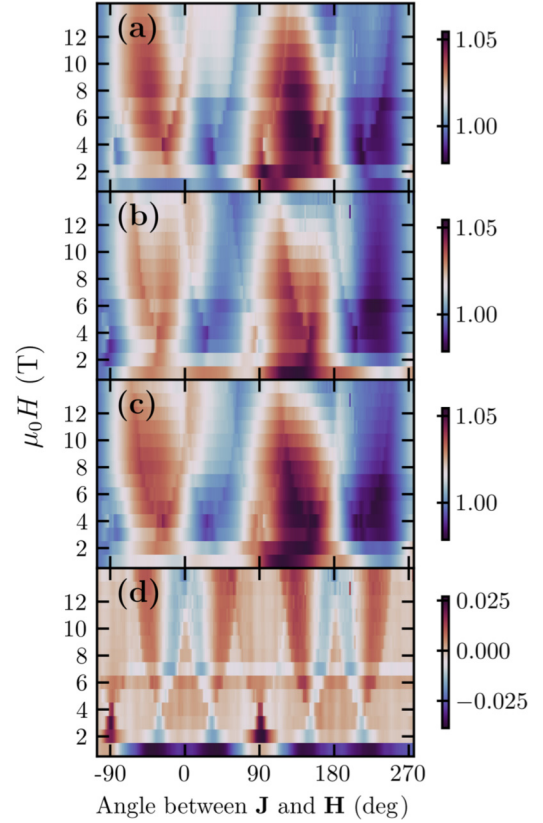


FIG. 16. PHE, $\rho_{xy}(\psi)/\rho_{xy}(\psi = 0)$ for (a) ψ increasing, (b) ψ decreasing, (c) the average of increasing and decreasing, and (d) the difference between increasing and decreasing.

vergence of 10^{-6} eV. Ground-state lattice constants were obtained by relaxing the atomic positions and cell size and shape.

B. Results

We performed DFT simulations on three ordered phases of Mn_3Ge : the $D0_{19}$ structure with AFM order and the cubic $L1_2$ phase with both AFM and FM orders. For the cubic

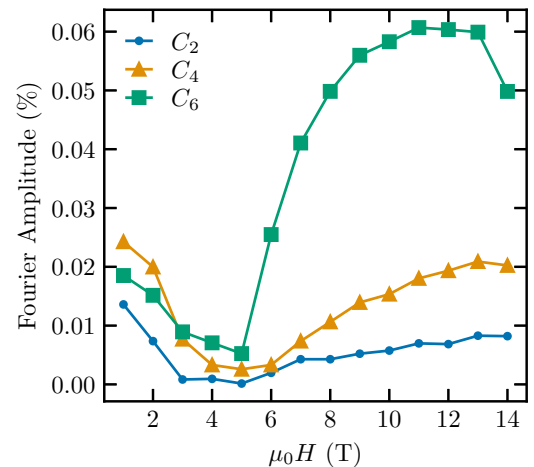


FIG. 17. Relative Fourier component amplitudes of the difference in the angle-increasing AMR and angle-decreasing AMR as a function of the applied field at 5 K.

TABLE I. DFT-computed properties of Mn_3Ge . For the cubic AFM phase, the angle of the local moment represents the average with values ranging between 84.30 and 84.40° . For the hexagonal phase, the two numbers correspond to the a and c lattice parameters. For the local magnetic moment, the first and second number correspond to the Mn and Ge components, respectively.

	Lattice constant (Å)	Local magnetic moment (μ_B)	Angle of local magnetic moment	Total magnetic moment (μ_B)	Angle of total magnetic moment	Energy/atom (eV)
Cubic AFM	3.707	2.446, 0.010	84.36° , 180° to [111]	0.760	0.04° to [111]	-8.040965
Hexagonal AFM	5.241, 4.229	2.291, 0.000	90.00° , -90.00° to [001]	0.014	89.68° to [001]	-8.027891
Cubic FM	3.641	1.691, 0.116	0° , 180° to [100]	5.216	0° to [100]	-7.986951

AFM phase, we considered the T_{1g} chiral AFM structure shown in Fig. 1(e) that is reported in the other $L1_2$ cubic AFMs [7,34–36]. We found that the local magnetic moment of Mn is $2.446 \mu_B$ with an average angle of 84.36° relative to the [111] direction [small canting out of the (111) plane], as shown in Table I. The angles of the Mn moments are found to vary slightly between 84.30° and 84.40° . This out-of-plane tilting leads to a total magnetic moment of $0.76 \mu_B$ aligned 0.04° relative to the [111] direction. A strained cubic lattice, converted into a hexagonal cell, was also tested based on experimental estimates of the lattice constants $a = 5.390 \text{ \AA}$ and $c = 6.285 \text{ \AA}$. The calculated local magnetic moments and their average orientation relative to the c axis (equivalent to the [111] direction in the cubic cell) are $2.565 \mu_B \text{ Mn}^{-1}$ and 88.51° , which represents an increase of $\approx 5\%$. There is also an energy increase of 17 meV/atom with the strained cell.

For the hexagonal phase, we used the E_{1g} antichiral spin structure determined by spherical neutron polarimetry, Fig. 1(b) [37]. Our DFT-calculated lattice parameters for the hexagonal AFM phase are within 2% of the experimental values of $a = 5.339\text{--}5.347 \text{ \AA}$ and $c = 4.314 \text{ \AA}$ [18]. The hexagonal AFM structure exhibits a measured local magnetic moment of $2.65(2) \mu_B \text{ Mn}^{-1}$ [37], which is higher than our value of $2.291 \mu_B \text{ Mn}^{-1}$. In another DFT study [38], a theoretical value of $2.7 \mu_B \text{ Mn}^{-1}$ was obtained using the experimental lattice constants and the local density approximation for exchange correlation. When adopting the same lattice parameters, we obtain a magnetic moment of $2.569 \mu_B \text{ Mn}^{-1}$, in closer agreement with the experimental value.

The spin-configuration used for the cubic phase with a FM order is shown in Fig. 1(c). The DFT-computed lattice constant is $\approx 4\%$ smaller than the value reported in bulk samples, 3.81 \AA , and our magnetic moment is not in good agreement with the value of $0.87 \mu_B \text{ Mn}^{-1}$ [23]. It should be noted that Ge exhibits a local magnetic moment that is aligned opposite to that of Mn, suggesting that this phase is ferrimagnetic.

Energetically, the cubic AFM phase is the lowest energy configuration, as shown in Fig. 18, followed by hexagonal AFM with an additional energy of 13 meV/atom and cubic FM with an additional energy of 54 meV/atom . Finally, we note that when the cell shape was allowed to change, each phase showed a tiny structural distortion leading to a negligible change in the properties of Mn_3Ge .

To compare with the momentum-space Berry curvature resulting in the AHE in the cubic Mn_3Ir and Mn_3Pt , the open-source WANNIER90 [39] was used to calculate the

anomalous Hall vector of the cubic AFM spin-configuration described previously. For the Berry curvature calculation, semicore states were included in the Wannierization process. This resulted in 72 maximally localized Wannier functions. A uniform, $200 \times 200 \times 200$ k -point mesh was used for the Brillouin-zone integration of the static anomalous Hall conductivity. The calculation indicates the presence of an intrinsic anomalous Hall vector with a magnitude of 155.7 S/cm at the Fermi level of the stoichiometric system. The Hall vector is directed along the [111] crystallographic direction, consistent with calculations completed for Mn_3Ir and Mn_3Pt .

VI. DISCUSSION

While the $M(H)$ loops in Fig. 7(a) are qualitatively similar to those of the bulk crystals reported in Ref. [23], with comparable values of M_S , our other results do not support the claim that the $\text{Mn}_{3.2}\text{Ge}$ films exhibit simple ferromagnetism. The average moment of $0.98 \mu_B \text{ Mn}^{-1}$ is only 58% of the DFT calculated value. The reversal of the remanent moment at a compensation point $T = 260 \text{ K}$ indicates that there are at least two different magnetic sites in the crystal that are coupled antiferromagnetically. The topological contribution to the Hall signal, evident from the different hysteretic behavior of $M(H)$ and ρ_{xy} in Fig. 8, indicates that these spins form a noncollinear configuration. Furthermore, the angular dependence of the PHE in Fig. 15 shows hysteresis up to at least 14 T, well above the apparent saturation field in the magnetometry measurements. This may be related to a competition between the

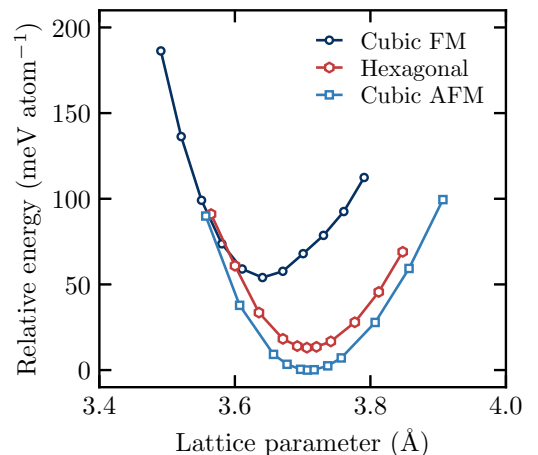


FIG. 18. The relative energy per atom of the three structures considered in the DFT simulations.

TABLE II. Hexagonal AFM Mn₃Ge. The lattice vectors are $a[1\ 0\ 0]$, $a[-1/2\ \sqrt{3}/2\ 0]$, $c[0\ 0\ 1]$, where $a = 5.241\ \text{\AA}$ and $c = 4.229\ \text{\AA}$. The total magnetic moment vector is $[-0.0035\ -0.0135\ 0.0000]\mu_B$. The atomic positions are expressed in terms of the lattice vectors.

	Atomic position	Local magnetic moment (μ_B)
Mn	(0.16133 0.32266 0.75000)	(0 2.291 0)
Mn	(0.83860 0.67734 0.25000)	(0 2.291 0)
Mn	(0.32266 0.16133 0.25000)	(1.982 -1.150 0)
Mn	(0.83860 0.16133 0.25000)	(-1.983 -1.147 0)
Mn	(0.67734 0.83867 0.75000)	(1.982 -1.150 0)
Mn	(0.16133 0.83867 0.75000)	(-1.983 -1.147 0)
Ge	(0.33333 0.66666 0.25000)	(0 0 0)
Ge	(0.66666 0.33333 0.75000)	(0 0 0)

magnetocrystalline anisotropy and the large exchange field between antiferromagnetically coupled spins. However, the results of these measurements are difficult to interpret without micromagnetic modeling and more detailed information about the atomic spin structure.

In addition to scalar spin chirality, there are likely significant contributions to the Hall effect from band structure topology. The low-temperature longitudinal conductivity $\sigma_{xx} = 3 \times 10^4\ \text{S/cm}$ places this material in the so-called *good-metal* regime, where intrinsic contributions to the AHE dominate [40]. It is interesting to note that the size of the Hall conductivity $\sigma_{xy} = 1587\ \text{S/cm}$ at $T = 50\ \text{K}$ is the highest reported for kagome magnets [41]: it is larger than the kagome ferromagnet Co₃Sn₂S₂ ($\sigma_{xy} = 1130\ \text{S/cm}$ [42]) and the frustrated kagome ferromagnet Fe₃Sn₂ ($\sigma_{xy} = 402\ \text{S/cm}$ [43]).

To understand the noncollinear structure it is important to consider the influence of chemical disorder. This disorder could be caused by the excess Mn in our films. The other report on cubic Mn₃Ge does not give any measure of the composition of the samples for us to compare with [23]. To find a point of reference, we turn to the $D0_{19}$ compounds. Excess Mn is commonly used to help stabilize the Mn₃Ge hexagonal phase, but for low enough concentrations, this does not destroy the chiral antiferromagnetic structure: the 120° inverse triangular structure was found for $D0_{19}$ Mn_{3,1}Ge [19] and Mn_{3,34}Sn [44]. At higher concentrations, glassy magnetic behavior can appear, as found for $D0_{19}$ Mn_{3,44}Sn [45], which shows a bifurcation between the zero-field-cooled and field-

TABLE III. Cubic AFM Mn₃Ge. The lattice vectors are $a[1\ 0\ 0]$, $a[0\ 1\ 0]$, $a[0\ 0\ 1]$, where $a = 3.707\ \text{\AA}$. The total magnetic moment vector is $[0.4387\ 0.4386\ 0.4394]\mu_B$. The atomic positions are expressed in terms of the lattice vectors.

	Atomic position	Local magnetic moment (μ_B)
Mn	(0.0 0.5 0.5)	(-1.849 1.132 1.133)
Mn	(0.5 0.0 0.5)	(1.132 -1.850 1.132)
Mn	(0.5 0.5 0.0)	(1.134 1.134 -1.847)
Ge	(0.0 0.0 0.0)	(-0.006 -0.006 -0.006)

TABLE IV. Cubic FM Mn₃Ge. The lattice vectors are $a[1\ 0\ 0]$, $a[0\ 1\ 0]$, $a[0\ 0\ 1]$, where $a = 3.641\ \text{\AA}$. The total magnetic moment vector is $[5.2159\ 0.0004\ -0.0002]$. The atomic positions are expressed in terms of the lattice vectors.

	Atomic position	Local magnetic moment (μ_B)
Mn	(0.0 0.5 0.5)	(1.690 0 0)
Mn	(0.5 0.0 0.5)	(1.692 0 0)
Mn	(0.5 0.5 0.0)	(1.692 0 0)
Ge	(0.0 0.0 0.0)	(-0.116 0 0)

cooled M -vs- T data. This occurs in samples with residual resistivity ratios lower than four [46], which is comparable to our films.

Insight into the impact of disorder on the magnetic structure can be gained by comparing the $L1_2$ and $D0_{22}$ Mn₃Ge polytypes. In the case of disorder in a stoichiometric $L1_2$ phase, an exchange of Mn and Ge between the $1a$ and $3c$ sites drives the material towards the $D0_{22}$ phase. The Mn antisite defects would be expected then to couple antiferromagnetically to the $3c$ Mn. The change would try to drive a distortion of the structure along the $[100]$ direction. Surprisingly from Fig. 4, we see a small elongation along the $[100]$ direction, rather than the contraction expected from the $D0_{22}$ structure. However, the tetragonal phase is not as well matched to SiC(0001), which may be the reason that the system remains nearly cubic. The fact that the moment of the $D0_{22}$ phase is far less than what we observe is further evidence that this phase is not formed. Based on DFT, the Mn on the $3c$ sites would like to form a 120° chiral structure. However, the expected antiferromagnetic interaction between the Mn_{3 c} and Mn_{1 a} would cause a large canting of the Mn away from the (111) plane.

Future studies of the effects of excess Mn should be of great interest. Given that the DFT simulations predict that the stoichiometric compound should have a chiral AFM structure, the spin structure should be quite sensitive to chemical tuning. The material potentially offers the opportunity of creating frustration-stabilized skyrmions [47], or other textures such as those found in Fe₃Sn₂ [48,49].

VII. SUMMARY

We have successfully synthesized Mn_{3,2}Ge films with a cubic kagome structure. Our magnetometry and magneto-transport measurements indicate that this is an interesting topological material worthy of future exploration. The giant anomalous Hall conductivity is the largest reported so far for the kagome magnets, possibly due to topological features in the underlying kagome crystal structure. A noncoplanar spin structure is also likely contributing a real-space Berry curvature component to the AHE signal. Further improvements in film morphology could make this an attractive material for device applications given its above-room-temperature Curie temperature and giant Hall response.

Note added. Recently, the authors became aware of another recent publication showing successful growth of cubic

$L1_2$ Mn_3Ge thin-films on $SrTiO_3$ substrates with a Ru buffer layer [50].

ACKNOWLEDGMENTS

We acknowledge financial support from the Natural Science and Engineering Research Council (Canada). We would like to thank M. L. Plumer, B. W. Southern and A. Zelenskiy for helpful discussions. We thank L. Kreplak for assistance with AFM measurements and Christian Lupien for assistance

with transport measurements. Computational resources were provided by the Digital Research Alliance of Canada.

APPENDIX: DFT-COMPUTED ATOMIC STRUCTURE AND MAGNETIC MOMENTS

Tables II–IV show the DFT-computed atomic structure and magnetic moments of Mn and Ge in the three magnetic configurations considered.

-
- [1] K. Kuroda, T. Tomita, M.-T. Suzuki, C. Bareille, A. A. Nugroho, P. Goswami, M. Ochi, M. Ikhlas, M. Nakayama, S. Akebi, R. Noguchi, R. Ishii, N. Inami, K. Ono, H. Kumigashira, A. Varykhalov, T. Muro, T. Koretsune, R. Arita, S. Shin, T. Kondo *et al.*, *Nat. Mater.* **16**, 1090 (2017).
- [2] S. Nakatsuji, N. Kiyohara, and T. Higo, *Nature (London)* **527**, 212 (2015).
- [3] N. Kiyohara, T. Tomita, and S. Nakatsuji, *Phys. Rev. Appl.* **5**, 064009 (2016).
- [4] M. Ikhlas, T. Tomita, T. Koretsune, M.-T. Suzuki, D. Nishio-Hamane, R. Arita, Y. Otani, and S. Nakatsuji, *Nat. Phys.* **13**, 1085 (2017).
- [5] D. Hong, N. Anand, C. Liu, H. Liu, I. Arslan, J. E. Pearson, A. Bhattacharya, and J. S. Jiang, *Phys. Rev. Mater.* **4**, 094201 (2020).
- [6] K.-R. Jeon, B. K. Hazra, J.-K. Kim, J.-C. Jeon, H. Han, H. L. Meyerheim, T. Kontos, A. Cottet, and S. S. P. Parkin, *Nat. Nanotechnol.* **18**, 747 (2023).
- [7] I. Tomeno, H. N. Fuke, H. Iwasaki, M. Sahashi, and Y. Tsunoda, *J. Appl. Phys.* **86**, 3853 (1999).
- [8] H. Yasui, M. Ohashi, S. Abe, H. Yoshida, T. Kaneko, Y. Yamaguchi, and T. Suzuki, *J. Magn. Magn. Mater.* **104-107**, 927 (1992).
- [9] E. Krén, G. Kádár, L. Pál, J. Sólyom, P. Szabó, and T. Tarnóczy, *Phys. Rev.* **171**, 574 (1968).
- [10] S. Tomiyoshi and Y. Yamaguchi, *J. Phys. Soc. Jpn.* **51**, 2478 (1982).
- [11] S. Tomiyoshi, Y. Yamaguchi, and T. Nagamiya, *J. Magn. Magn. Mater.* **31-34**, 629 (1983).
- [12] Z. Q. Liu, H. Chen, J. M. Wang, J. H. Liu, K. Wang, Z. X. Feng, H. Yan, X. R. Wang, C. B. Jiang, J. M. D. Coey, and A. H. MacDonald, *Nat. Electron.* **1**, 172 (2018).
- [13] B. E. Zuniga-Cespedes, K. Manna, H. M. L. Noad, P.-Y. Yang, M. Nicklas, C. Felser, A. P. Mackenzie, and C. W. Hicks, *New J. Phys.* **25**, 023029 (2023).
- [14] W. Zhang, W. Han, S.-H. Yang, Y. Sun, Y. Zhang, B. Yan, and S. S. P. Parkin, *Sci. Adv.* **2**, 1600759 (2016).
- [15] H. Chen, Q. Niu, and A. H. MacDonald, *Phys. Rev. Lett.* **112**, 017205 (2014).
- [16] K. Momma and F. Izumi, *J. Appl. Crystallogr.* **41**, 653 (2008).
- [17] T. Ohoyama, *J. Phys. Soc. Jpn.* **16**, 1995 (1961).
- [18] N. Yamada, H. Sakai, H. Mori, and T. Ohoyama, *Physica B + C (Amsterdam)* **149**, 311 (1988).
- [19] G. Kádár and E. Krén, *Int. J. Magn.* **1**, 143 (1971).
- [20] D. Hong, C. Liu, J. Wen, Q. Du, B. Fisher, J. S. Jiang, J. E. Pearson, and A. Bhattacharya, *APL Mater.* **10**, 101113 (2022).
- [21] H. Kurt, N. Baadji, K. Rode, M. Venkatesan, P. Stamenov, S. Sanvito, and J. M. D. Coey, *Appl. Phys. Lett.* **101**, 132410 (2012).
- [22] A. Sugihara, S. Mizukami, Y. Yamada, K. Koike, and T. Miyazaki, *Appl. Phys. Lett.* **104**, 132404 (2014).
- [23] H. Takizawa, T. Yamashita, K. Uheda, and T. Endo, *J. Phys.: Condens. Matter* **14**, 11147 (2002).
- [24] A. Bauer, P. Reischauer, J. Kräusslich, N. Schell, W. Matz, and K. Goetz, *Acta Crystallogr., Sect. A: Found. Crystallogr.* **57**, 60 (2001).
- [25] M. D. Robertson, T. Burns, and T. Morrison, *Microsc. Soc. Can. Bull.* **34**, 19 (2006).
- [26] J. Humphreys, *Rep. Prog. Phys.* **42**, 1825 (1979).
- [27] D. Kriegner, E. Wintersberger, and J. Stangl, *J. Appl. Crystallogr.* **46**, 1162 (2013).
- [28] S. Meynell, A. Spritzig, B. Edwards, M. Robertson, D. Kalliecharan, L. Kreplak, and T. Monchesky, *Phys. Rev. B* **94**, 184416 (2016).
- [29] G. Kresse and J. Furthmüller, *Phys. Rev. B* **54**, 11169 (1996).
- [30] J. P. Perdew, K. Burke, and M. Ernzerhof, *Phys. Rev. Lett.* **77**, 3865 (1996).
- [31] G. Kresse and D. Joubert, *Phys. Rev. B* **59**, 1758 (1999).
- [32] H. J. Monkhorst and J. D. Pack, *Phys. Rev. B* **13**, 5188 (1976).
- [33] M. Methfessel and A. T. Paxton, *Phys. Rev. B* **40**, 3616 (1989).
- [34] E. Krén, G. Kádár, L. Pál, J. Sólyom, and P. Szabó, *Phys. Lett.* **20**, 331 (1966).
- [35] A. Sakuma, R. Y. Umetsu, and K. Fukamichi, *Phys. Rev. B* **66**, 014432 (2002).
- [36] T. Ikeda and Y. Tsunoda, *J. Phys. Soc. Jpn.* **72**, 2614 (2003).
- [37] J.-R. Soh, F. de Juan, N. Qureshi, H. Jacobsen, H.-Y. Wang, Y.-F. Guo, and A. T. Boothroyd, *Phys. Rev. B* **101**, 140411(R) (2020).
- [38] H. Yang, Y. Sun, Y. Zhang, W.-J. Shi, S. S. P. Parkin, and B. Yan, *New J. Phys.* **19**, 015008 (2017).
- [39] A. Mostofi, J. Yates, G. Pizzi, Y. Lee, I. Souza, D. Vanderbilt, and N. Marazi, *Comput. Phys. Commun.* **185**, 2309 (2014).
- [40] T. Miyasato, N. Abe, T. Fujii, A. Asamitsu, S. Onoda, Y. Onose, N. Nagaosa, and Y. Tokura, *Phys. Rev. Lett.* **99**, 086602 (2007).
- [41] T. Chen, T. Tomita, S. Minami, M. Fu, T. Koretsune, M. Kitatani, I. Muhammad, D. Nishio-Hamane, R. Ishii, F. Ishii, R. Arita, and S. Nakatsuji, *Nat. Commun.* **12**, 572 (2021).
- [42] E. Liu, Y. Sun, N. Kumar, L. Muechler, A. Sun, L. Jiao, S.-Y. Yang, D. Liu, A. Liang, Q. Xu, J. Kroder, V. Süß, H. Borrmann,

- C. Shekhar, Z. Wang, C. Xi, W. Wang, W. Schnelle, S. Wirth, Y. Chen *et al.*, *Nat. Phys.* **14**, 1125 (2018).
- [43] Q. Wang, S. Sun, X. Zhang, F. Pang, and H. Lei, *Phys. Rev. B* **94**, 075135 (2016).
- [44] G. J. Zimmer and E. Krén, in *Eighteenth Annual Conference on Magnetism and Magnetic Materials 1972*, AIP Conf. Proc. No. 10 (AIP, New York, 1973), pp. 1379–1383.
- [45] W. J. Feng, D. Li, W. J. Ren, Y. B. Li, W. F. Li, J. Li, Y. Q. Zhang, and Z. D. Zhang, *Phys. Rev. B* **73**, 205105 (2006).
- [46] M. Ikhlas, T. Tomita, and S. Nakatsuji, *J. Phys. Soc. Jpn.* **30**, 011177 (2020).
- [47] A. O. Leonov and M. Mostovoy, *Nat. Commun.* **6**, 8275 (2015).
- [48] K. Kuroda, T. Tomita, M.-T. Suzuki, C. Bareille, A. A. Nugroho, P. Goswami, M. Ochi, M. Ikhlas, M. Nakayama, S. Akebi, R. Noguchi, R. Ishii, N. Inami, K. Ono, H. Kumigashira, A. Varykhalov, T. Muro, T. Koretsune, R. Arita, S. Shin, T. Kondo, *Adv. Mater.* **29**, 1701144 (2017).
- [49] Q. Du, Z. Hu, M.-G. Han, F. Camino, Y. Zhu, and C. Petrovic, *Phys. Rev. Lett.* **129**, 236601 (2022).
- [50] A. Markou, J. M. Taylor, J. Gayles, Y. Sun, D. Kriegner, J. Grenzer, S. Guo, W. Schnelle, E. Lesne, C. Felser, and S. S. P. Parkin, *Appl. Phys. Lett.* **125**, 022402 (2024).